STRUCTURAL BIOLOGY

Structural basis for C-type inactivation in a Shaker family voltage-gated K$^+$ channel

Ravikumar Reddi[1], Kimberly Matulef[1], Erika A. Riederer[1], Matthew R. Whorton[2], Francis I. Valiyaveetil[1]*

C-type inactivation is a process by which ion flux through a voltage-gated K$^+$ (K$_v$) channel is regulated at the selectivity filter. While prior studies have indicated that C-type inactivation involves structural changes at the selectivity filter, the nature of the changes has not been resolved. Here, we report the crystal structure of the K$_v$1.2 channel in a C-type inactivated state. The structure shows that C-type inactivation involves changes in the selectivity filter that disrupt the outer two ion binding sites in the filter. The changes at the selectivity filter propagate to the extracellular mouth and the turret regions of the channel pore. The structural changes observed are consistent with the functional hallmarks of C-type inactivation. This study highlights the intricate interplay between K$^+$ occupancy at the ion binding sites and the interactions of the selectivity filter in determining the balance between the conductive and the inactivated conformations of the filter.

INTRODUCTION

Voltage-gated K$^+$ channels (K$_v$) are essential for the generation and conduction of electrical signals by neurons, muscle, and endocrine cells (1). K$_v$ channels are tetrameric proteins that contain a central pore domain and peripheral voltage sensor domains (VSDs; Fig. 1A) (2, 3). The pore domain houses the pathway for K$^+$ ions across the membrane (Fig. 1B). The activation of a K$_v$ channel takes place upon membrane depolarization and involves an outward movement of the VSDs (4). This movement of the VSD is coupled to the opening of the pore domain to turn on the K$^+$ flux across the membrane. On sustained activation, the flux of K$^+$ through the K$_v$ channel is turned off through mechanisms that are referred to as inactivation (5).

In the Shaker family of K$_v$ channels, there are two types of inactivation, N-type and C-type (6, 7). In N-type inactivation, the N terminus of the channel binds to the open pore domain and occludes the ion pathway (6, 8, 9). Shaker channels with the N terminus deleted do not undergo N-type inactivation but inactivate through a different mechanism called C-type inactivation (7). This mechanism is also referred to as slow inactivation as the time scale is generally slower, on the order of seconds, compared to the millisecond time scale observed for N-type inactivation (10). C-type inactivation is a physiologically important process that can regulate cell excitability by determining channel availability (11, 12).

The mechanism of C-type inactivation has been investigated using functional, spectroscopic, structural, and computational approaches (5). All these approaches suggest that C-type inactivation involves changes at the selectivity filter. The selectivity filter refers to the narrow region of the ion pathway in the pore domain, where selection for K$^+$ takes place (Fig. 1C) (13). The selectivity filter consists of a row of K$^+$ binding sites (called S1 to S4, extracellular to intracellular) that are constructed from the main-chain carbonyl atoms and the threonine side chain from the protein sequence T-V-G-Y-G (14). The structures of the selectivity filter of K$^+$ channels are highly conserved. The structures determined mainly show the selectivity filter in a conductive state, the state of the selectivity filter that supports the flux of K$^+$ through the channel. During C-type inactivation, there are structural changes at the selectivity filter that convert the selectivity filter from a conductive to a nonconductive conformation (5, 10).

Understanding the mechanism of C-type inactivation requires the structure of the selectivity filter in the C-type inactivated state. The structure of a nonconducting mutant of the K$_v$1.2 channel has been proposed to show the selectivity filter in the C-type inactivated state (15). However, the structural changes observed were minimal, which raises a question on whether this structure truly represents the C-type inactivated state (16). Other structural studies on C-type inactivation have used the K$^+$ channel KcsA. KcsA does not belong to the K$_v$ family but undergoes an inactivation process that bears some functional similarity to C-type inactivation in K$_v$ channels (17). Structural studies on the KcsA channel under conditions that favor inactivation show a constriction of the selectivity filter (18, 19). However, the relevance of this constricted conformation to C-type inactivation in K$_v$ channels has been debated (20).

Here, we report the crystal structure of the K$_v$1.2 channel in the C-type inactivated state. We carry out structural studies on a mutant of the K$_v$1.2 channel that shows a vastly increased rate of C-type inactivation. We observe that C-type inactivation involves a dilation of the outer ion binding sites of the selectivity filter along with changes in the extracellular mouth and the turret regions of the pore domain. Our studies highlight the selectivity filter interactions that are important for C-type inactivation and suggest a molecular pathway for this process.

RESULTS

C-type inactivation in the K$_v$1.2-2.1 channel

A feature of C-type inactivation is that it is enhanced at low K$^+$ (21, 22). To elucidate the structural changes in the K$_v$1.2 channel during C-type inactivation, we initially attempted structural studies of the K$_v$1.2 channel at low K$^+$. These attempts were unsuccessful as the K$_v$1.2 channel was recalcitrant to crystallization at low K$^+$. We therefore pursued a strategy of using mutants of the channel that show an

[1]Program in Chemical Biology, Department of Chemical Physiology and Biochemistry, Oregon Health & Science University, 3181 SW Sam Jackson Park Rd, Portland, OR 97239, USA. [2]Vollum Institute, Oregon Health & Science University, 3181 SW Sam Jackson Park Rd, Portland, OR 97239, USA.
*Corresponding author. Email: valiyave@ohsu.edu
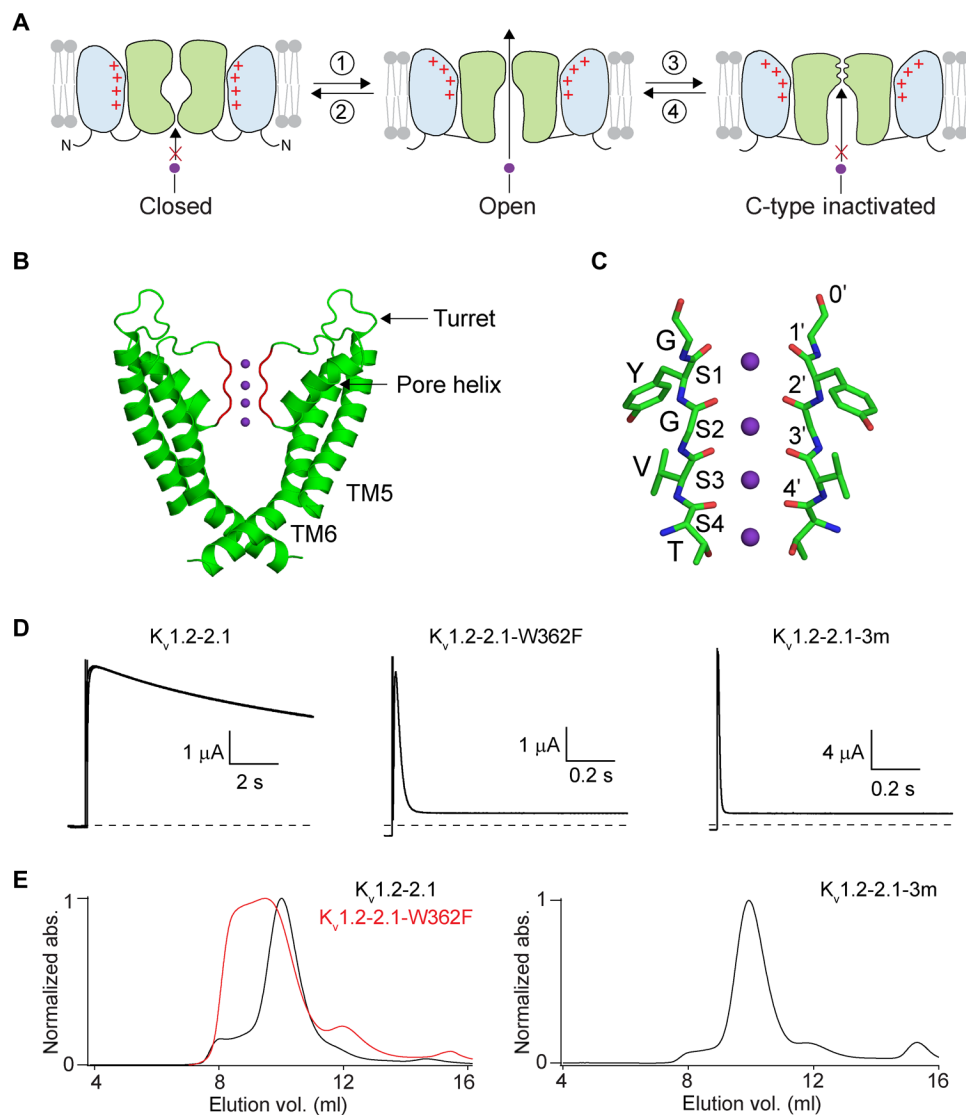
Fig. 1. C-type inactivation in the K_v1.2-2.1 channel. (**A**) Gating mechanisms in K_v channels. The gating processes in a K_v channel of activation (1), deactivation (2), C-type inactivation (3), and recovery from inactivation (4) are depicted. TM4 in the VSD is colored red. Voltage gating involves the movement of the TM4 helix, while C-type inactivation involves structural changes at the selectivity filter. (**B**) The pore domain of the K_v1.2-2.1 channel (pdb: 2r9r). Two opposite subunits are shown, with the selectivity filter colored red and the K^+ ions bound at the selectivity filter depicted as purple spheres. (**C**) Close-up view of the selectivity filter of the K_v1.2-2.1 channel. Two opposite subunits are shown in stick representation. The ion binding sites in the selectivity filter (S1 to S4) and the 0' to 4' carbonyl bonds are labeled. (**D**) C-type inactivation in the K_v1.2-2.1, K_v1.2-2.1-W362F, and K_v1.2-2.1-3m channels. Time course of current elicited by stepping the voltage from −80 mV holding potential to 40 mV with 100 mM external K^+. Initial spikes observed are the capacitance transients. Currents are presented without leak subtraction, and the zero current level is indicated by a dashed line. The inactivation time constants determined were 11,890 ± 1666 ms (±SEM, $n = 4$) for K_v1.2-2.1, 22.4 ± 7.2 ms ($n = 9$) for the K_v1.2-2.1-W362F, and 5.5 ± 0.7 ms ($n = 10$) for the K_v1.2-2.1-3m channels. (**E**) Size exclusion chromatography profiles of the purified K_v1.2-2.1, K_v1.2-2.1-W362F, and the K_v1.2-2.1-3m channel. abs., absorbance.

enhanced rate of inactivation with the expectation that these mutants will trap the selectivity filter in the C-type inactivated state. In the Shaker channel, the W434F substitution markedly increases the rate of inactivation, and this substitution has been extensively used in functional studies to mimic the C-type inactivated state (23). The corresponding mutation, W366F in the K_v1.2 channel, has been shown to have an increased rate of inactivation (fig. S1) (24, 25). For our studies, we used a variant of the K_v1.2 channel referred to as the K_v1.2-2.1 chimera (referred henceforth as K_v1.2-2.1) as this construct affords crystals that diffract to a higher resolution (3). In the K_v1.2-2.1 channel, residues 267 to 302 in the S3-S4 loop in the VSD

are substituted by residues 274 to 305 of the K_v2.1 channel. The K_v1.2-2.1 channel shows similar functional properties to the K_v1.2 channel, and the W362F (equivalent to W366F in K_v1.2) substitution in the K_v1.2-2.1 channel shows a similar enhancement in the rate of inactivation (Fig. 1D) (26).

Our attempts at structural studies of the K_v1.2-2.1-W362F channel were stymied as the channel showed poor expression and suboptimal biochemistry (Fig. 1E). We therefore screened for additional amino acid substitutions that improved protein expression and biochemical behavior while maintaining an enhanced rate of C-type inactivation. These efforts identified a construct with two additional

substitutions, S367T and V377T, which exhibited good biochemical behavior and an enhanced rate of inactivation (Fig. 1, D and E). Previous studies on the $K_v1.2$ channel have indicated that the equivalent substitution S371T (S367T in $K_v1.2$-2.1) enhances cell surface expression, while V381T (V377T in $K_v1.2$-2.1) markedly enhances the rate of C-type inactivation in the W366F-$K_v1.2$ channel (25, 27, 28). We refer to the $K_v1.2$-2.1 channel with the W362F, S367T, and V377T substitutions as the $K_v1.2$-2.1-3m channel. At high (100 mM) K^+, the $K_v1.2$-2.1-3m channel showed a ~2000-fold increase in the rate of C-type inactivation, while at low (1 mM) external K^+, the rate of C-type inactivation was very fast and could not be accurately determined (Fig. 1D and fig. S2). On the basis of the rapid rate of inactivation, we anticipated that the crystal structure of the $K_v1.2$-2.1-3m channel would reveal the selectivity filter in the C-type inactivated state.
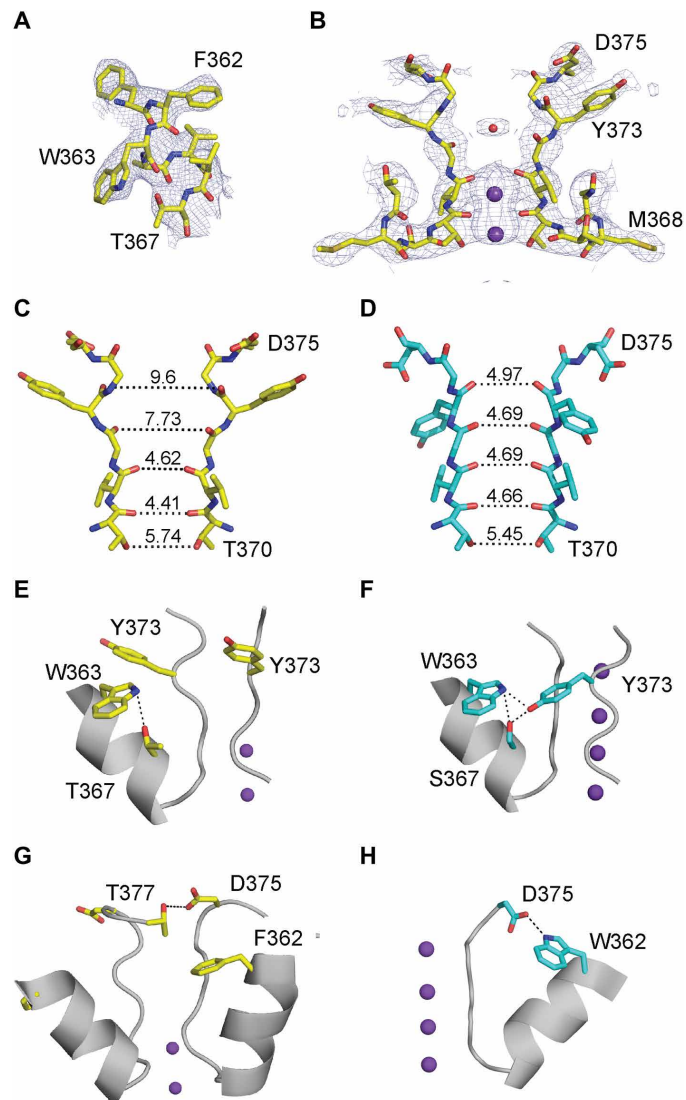
Structure of the $K_v1.2$-2.1-3m channel

For structural studies, the $K_v1.2$-2.1-3m channel was coexpressed with the β subunit, and the channel-β complex was crystallized in the presence of 150 mM K^+. We obtained crystals of the same space group ($P4\,2_1\,2$) as reported for the $K_v1.2$-2.1 channel but with slightly altered unit cell parameters (3). Data from multiple crystals were combined to obtain a complete dataset to 3.35-Å resolution, and the structure was determined by molecular replacement using the $K_v1.2$-2.1 [Protein Data Bank (PDB): 2r9r] channel structure as the model (table S1). There are two copies (molecules I and II) of the channel-beta complex in the asymmetric unit. The β subunit and the T1 domain in both molecules were well resolved, while the transmembrane (TM) region in molecule I was better resolved than in molecule II. For the TM region, we observed stronger electron density for the pore domain compared to the VSD. Within the pore domain, the electron density for Y373-D375 was weaker compared to the neighboring residues, and electron density for the carbonyl group for the G374 residue was not observed. Electron density corresponding to the pore helix and the selectivity filter are shown in Fig. 2 (A and B) and in fig. S3. In the VSD, the electron density was sufficient for modeling the TM segments (fig. S4), while electron density for the loops connecting the TM segments and the linker connecting the T1 domain to the first TM segment was not observed, and these regions were therefore not modeled. A superposition of the various domains in the $K_v1.2$-2.1-3m channel to $K_v1.2$-2.1 channel shows that the structural changes observed are mainly in the pore domain (fig. S5). Changes are observed in the orientation of the VSD with respect to the pore domain (fig. S5). Within the pore domain, the structural changes are mainly in the selectivity filter region and in the extracellular mouth of the pore (figs. S5 and S6).

The selectivity filter in the $K_v1.2$-2.1-3m channel

A comparison of the selectivity filter in $K_v1.2$-2.1-3m to the wild-type channel shows substantial changes in the side-chain and backbone conformations (Fig. 2, C and D). A major change observed is a reorientation of the Tyr side chain (Fig. 2, E and F, and fig. S3A). In the $K_v1.2$-2.1 channel, the Tyr side chain interacts with the Trp[363] and Ser[367] of the adjacent subunit, while in the $K_v1.2$-2.1-3m channel, these H-bond interactions are broken, the Tyr side chain undergoes a 77° rotation, and the hydroxyl group in the Tyr side chain is now oriented toward the extracellular surface.

Another major change observed in the $K_v1.2$-2.1-3m channel is a flip of the Asp[375] side chain (Fig. 2, G and H, and fig. S3B). In the

Fig. 2. Changes in the selectivity filter on C-type inactivation. (**A**) The pore helix of the $K_v1.2$-2.1-3m channel. The $2F_{obs}$-F_{calc} electron density map contoured at 1.4σ is shown with residues 361 to 367 as sticks. The W362F and S367T substitutions present in the $K_v1.2$-2.1-3m channel are indicated. (**B**) The selectivity filter of the $K_v1.2$-2.1-3m channel. The $2F_{obs}$-F_{calc} electron density map contoured at 0.9σ is shown with residues 368 to 375 as sticks, K^+ ions as purple spheres, and water molecule as a red sphere. (**C** and **D**) Comparison of the selectivity filter of the $K_v1.2$-2.1-3m (C) and the $K_v1.2$-2.1 channel (D). Residues 370 to 375 are shown as sticks. The distance (in angstroms) between the carbonyl oxygens and the Thr[370] side-chain hydroxyl group in the opposite subunits is indicated by dotted lines. (**E** to **H**) Close-up of the selectivity filter and the pore helix showing the Y373 side chain in the $K_v1.2$-2.1-3m (E) and $K_v1.2$-2.1 channel (F) and the D375 side chain in the $K_v1.2$-2.1-3m (G) and $K_v1.2$-2.1 channel (H).

$K_v1.2$-2.1 structure, Asp[375] forms a H bond with Trp[362] in the pore helix. This H bond is disrupted in the $K_v1.2$-2.1-3m channel because of the W362F substitution. The Asp[375] side chain is now oriented toward the extracellular solution and forms a H bond with Thr[377] in the adjacent subunit (distance of 3.2 Å). The $K_v1.2$-2.1 channel has a Val at this position, which is substituted by Thr in the $K_v1.2$-2.1-3m channel. The flip of the Asp side chain as observed

changes the side chain from being oriented toward the channel interior (in K_v1.2-2.1) to facing the extracellular solution.

The changes in the Tyr[373] and Asp[375] side-chain conformations cause a widening of the selectivity filter toward the extracellular side. Because of this widening, the S1 and S2 ion binding sites are disrupted and instead form a vestibule (Fig. 2, C and D). In K_v1.2-2.1, K^+ binding is observed at the S1 and the S2 sites, while in the K_v1.2-2.1-3m channel, only a weak electron density is observed in this vestibule region (Fig. 2B and fig. S7). The electron density in vestibule region can correspond to either a low-occupancy K^+ ion or a water molecule. The distances between the carbonyl oxygens in the vestibule region are, however, too large to tightly coordinate either a water or a K^+ ion. In contrast to the changes seen at the S1 and the S2 sites, the S3 and the S4 sites in the K_v1.2-2.1-3m filter are well superimposed on the corresponding sites in the K_v1.2-2.1 filter, and electron density corresponding to ion binding at these sites is observed. Previous studies have implicated the outer sites in the selectivity filter in C-type inactivation (29, 30), and the K_v1.2-2.1-3m structure indicates that inactivation involves a disruption of the S1 and the S2 sites in the selectivity filter. Occupancy of the S1 and the S2 sites will increase with K^+ concentration. If the S1 or the S2 sites are occupied by K^+, then the presence of the ion will slow structural changes at these sites and thereby affect C-type inactivation. The structure therefore provides a potential mechanism for the effect of extracellular K^+ on C-type inactivation (21, 22).

Changes in the extracellular mouth of the K_v1.2-2.1-3m pore

The changes in the selectivity filter in the K_v1.2-2.1-3m structure are propagated to the loop region linking the selectivity filter to TM6 (Fig. 3A). The changes observed in this region are mainly due to the repositioning of the Asp[375] side chain (Fig. 3, B and C). Studies on the Shaker K^+ channel have shown that Cys substitutions at positions 448 to 450, equivalent to positions 376 to 378 in the K_v1.2-2.1-3m channel, show different rates of modification by thiol reagents in the conductive versus the inactivated state (31). Studies on Shaker have also shown that a Cys substitution at 448 (376 in K_v1.2-2.1-3m) exhibits an enhanced rate of formation of a disulfide bond, while a Cys substitution at 449 (377 in K_v1.2-2.1-3m) can form a high-affinity metal (Cd^{2+} or Zn^{2+})–binding site in the inactivated state (31, 32). Comparison of the 376 to 378 region in the K_v1.2-2.1-3m to the K_v1.2-2.1 shows an increase in surface exposure of these residues (fig. S8), which may underlie the changes in modification observed (for Cys substitutions at these sites) on C-type inactivation. In the K_v1.2-2.1-3m structure, the Cα-Cα distance between the 376 side chains in the adjacent subunits is similar to the distance observed in the K_v1.2-2.1 structure (Fig. 3, B and C). The K_v1.2-2.1-3m structure therefore does not account for the enhanced rate of disulfide bond formation by Cys[376] in the C-type inactivated state. Similarly, the change in the Cα-Cα distance of the 377 side chains in these structures is 0.51 Å (14.06 to 13.55 Å), and this distance is still longer than expected for the formation of a metal coordination site by the Cys[377] side chains from adjacent subunits (33). The K_v1.2-2.1-3m channel structure therefore does not directly account for some of the changes in the extracellular mouth of the pore on C-type inactivation as inferred from the functional studies. One possibility is that the full extent of changes in the extracellular mouth of the pore on C-type inactivation is not revealed in the K_v1.2-2.1-3m structure. Another possibility is that these experimental findings reflect greater flexibility in the extracellular mouth of the channel in the C-type
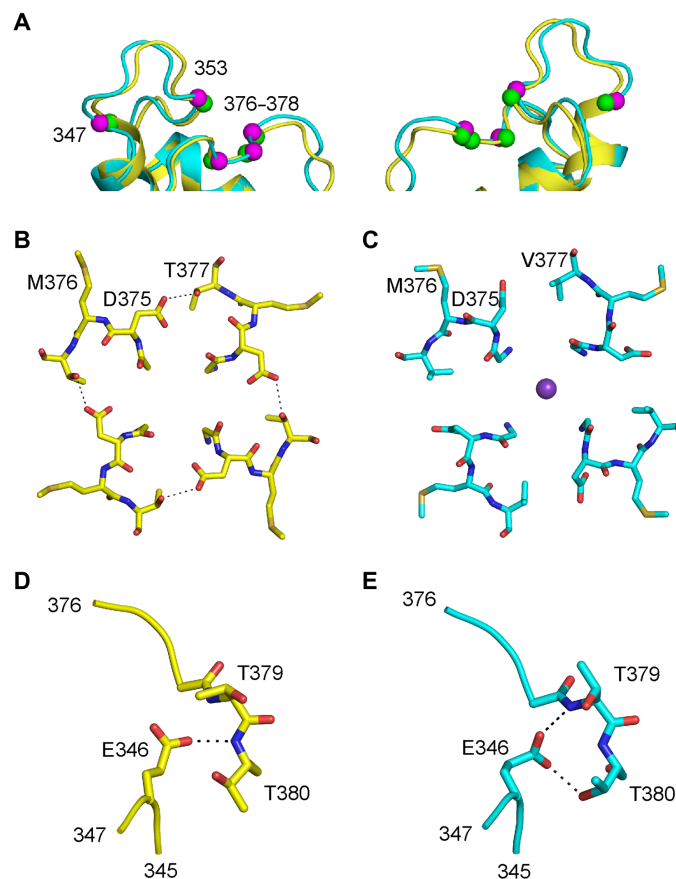
Fig. 3. The outer pore region in the C-type inactivated channel. (**A**) Superposition of the outer pore region of the K_v1.2-2.1-3m (yellow) and the K_v1.2-2.1 channel (cyan). Two opposite subunits are shown. Some of the positions at which fluorescence probes introduced detected structural changes on C-type inactivation are indicated (green spheres in K_v1.2-2.1-3m and magenta spheres in K_v1.2-2.1). (**B** and **C**) Top view of the extracellular mouth of the pore in the K_v1.2-2.1-3m (B) and the K_v1.2-2.1 channel (C) shows changes in conformation of D375 and M376. The H-bond interaction between D375 and T377 in adjacent subunits of the K_v1.2-2.1-3m channel is shown. (**D** and **E**) H-bond interactions of E346 in K_v1.2-2.1-3m (D) and K_v1.2-2.1 channel (E) are shown.

inactivated state. An increased flexibility in the extracellular mouth on C-type inactivation could explain the weaker electron density observed in the Y373-D375 region in the K_v1.2-2.1-3m channel.

Binding of Tetraethylammonium (TEA) to the extracellular mouth of the pore slows C-type inactivation in the Shaker channel, and a similar effect has been demonstrated in the K_v1.2 channel (25, 34). We anticipate that TEA binding will hinder the conformational change observed in the extracellular mouth of the pore and thereby affect C-type inactivation.

C-type inactivation also involves changes in the turret region present between TM5 and the pore helix. Fluorescent probes introduced into the turret region show a change in fluorescence on C-type inactivation (35–37). We see structural changes in the turret region of the K_v1.2-2.1-3m corresponding to the sites of introduction of the fluorescence probes (Fig. 3A and fig. S9A). A key interaction that is altered in the K_v1.2-2.1-3m channel is that of the E346 residue, which is toward the top of TM5 (Fig. 3, D and E, and fig. S9B). Mutations at this Glu (E418 in the Shaker channel) increase

the rate of inactivation (*37, 38*). In the K$_v$1.2-2.1 channel, E346 interacts with the pore-S6 loop region of the channel through H-bond interactions with the protein backbone of Thr[379] and the side chain of Thr[380]. In the K$_v$1.2-2.1-3m structure, we observe a change in the E346 side-chain conformation with the H-bond interactions to the protein backbone of Thr[379] and the side chain of Thr[380] broken, and a new H bond formed with the protein backbone of Thr[379].

Structure of the K$_v$1.2-2.1-W362F and S367T channel

To test the importance of the interaction between Asp[375] and Thr[377] for C-type inactivation, we investigated the functional properties of a K$_v$1.2-2.1 channel with the native Val at 377 along with the W362F and S367T substitution (referred to as K$_v$1.2-2.1-2m). We observed that the inactivation in this mutant was slow compared to the very rapid inactivation observed in the K$_v$1.2-2.1-3m channel. Inactivation in the K$_v$1.2-2.1-2m channel was similar to the inactivation observed in the K$_v$1.2-2.1 channel (Fig. 4A). We crystallized and determined the structure of the K$_v$1.2-2.1-2m channel at 150 mM K$^+$ (Fig. 4B and table S1). In the K$_v$1.2-2.1-2m structure, we observed the selectivity filter in a conductive conformation as anticipated on the basis of the similarity of the inactivation properties of the K$_v$1.2-2.1-2m to the K$_v$1.2-2.1 channel (Fig. 4C). These findings suggest a role for the intersubunit Asp[375]-Thr[377] interaction in stabilizing the selectivity filter in the C-type inactivated state. The equivalent position in the Shaker channel (Thr[449]) is an important locus for C-type inactivation, and substitution of T449 in the Shaker channel with Val results in a noninactivating phenotype (*21*). Our studies suggest that substitutions at this site affect C-type inactivation through an effect on the interaction with the Asp residue.

DISCUSSION

Here, we report the structure of the K$_v$1.2 channel in the C-type inactivated state (Fig. 5A). The structure shows that the C-type inactivation involves a dilation of the selectivity filter at the S1 and S2 ion binding sites, which is caused by structural changes at the conserved Tyr and Asp side chains (movie S1). The disruption of the S1 and the S2 ion binding sites of the filter perturbs K$^+$ flux through the channel. The structure shows that the changes in the selectivity filter on C-type inactivation are propagated to the extracellular mouth and the turret region of the pore domain of the channel (movie S2). The structure of the selectivity filter in the C-type inactivated state is consistent with the dilation model for inactivation previously proposed by Hoshi and Armstrong (*10*). Multiple amino acid

substitutions were necessary to stabilize the C-type inactivated state and to improve the biochemical behavior for structure determination. While we anticipate that the structural changes observed correspond to the changes in the K$_v$1.2 channel during C-type inactivation, it is feasible that the nature and magnitude of the structural changes observed are influenced by the amino acid substitutions present in the crystallized construct.

A structure of the K$_v$1.2-2.1-V406W channel has been reported as presenting the selectivity filter in the C-type inactivated state (fig. S10) (*15*). The structural change observed in the selectivity filter, compared to the conductive state, is a small distortion of the S1 site (*16*). This is in contrast to the abrogation of the S1 and S2 sites observed in the K$_v$1.2-2.1-3m structure. The proposed inactivated state in the KcsA channel shows a distortion of the S2 and the S3 sites of the selectivity filter and is distinct from the structure of the selectivity filter in the K$_v$1.2-2.1-3m channel (fig. S10). Gating of K$^+$ flux through two-pore K$^+$ (K2P) channels takes place at the selectivity filter by a mechanism that shares a functional resemblance to C-type inactivation in K$_v$ channels (*39*). A recent structural study on the TREK-1 K2P channel suggested that the gating process involves a loss of the S1 and the S2 ion binding sites in the selectivity filter, while a structure of the TASK 2-P K$^+$ channel indicated a loss of the S1 (and potentially the S0) binding site in the inactivated state (*40, 41*). These structures suggest that K$^+$ channels, which have essentially identical selectivity filters, can have distinct mechanisms of inactivation or gating at the selectivity filter.

A structure of the W434F mutant of the Shaker K$^+$ channel was recently reported (Fig. 5B) (*42*). The selectivity filter in the W434F Shaker channel shows a dilation of the S1 and S2 sites and a flip of the Tyr residue, similar to the changes observed in the K$_v$1.2-2.1-3m channel (Fig. 5C). There are differences between these structures in the conformation of the Asp residue and in the loop region with a different conformation observed for the Met and Thr side chains (Fig. 5D). Furthermore, the interaction between Asp and Thr in the neighboring subunits seen in K$_v$1.2-2.1-3m is not observed in the W434F Shaker structure, and the Asp residue potentially interacts with the Thr side chain in the same subunit. These changes in the inactivated state structures are modest but may be responsible for the reported differences in the inactivation properties of the K$_v$1.2 and the Shaker channel (*25*).

C-type inactivation is widespread in the K$_v$ channel family with the inactivation properties that are tuned for the specific physiological roles of these channels (*43*). Structural studies of these other K$_v$ family members will be necessary to determine whether
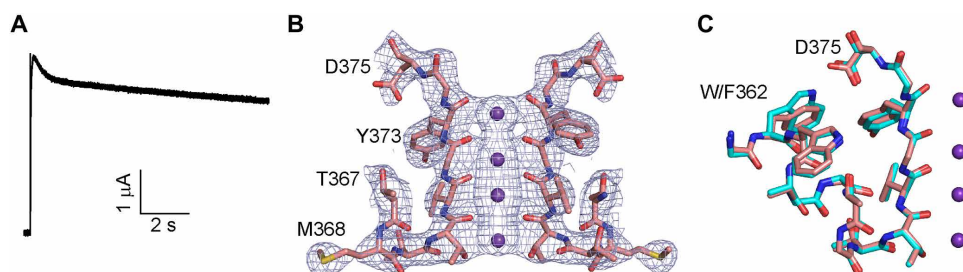
Fig. 4. Structure of the selectivity filter in the K$_v$1.2-2.1-2m channel. (**A**) C-type inactivation in the K$_v$1.2-2.1-2m (W362F and S367T) channel. Time course of the current elicited by stepping the voltage from −80 mV holding potential to 40 mV in 100 mM external K$^+$. (**B**) Electron density of the selectivity filter of K$_v$1.2-2.1-2m. The 2F_o-F_c electron density map contoured at 1.3σ is shown with residues 367 to 375 as sticks, and the K$^+$ ions in the selectivity filter shown as purple spheres. (**C**) Superposition of the pore helix and filter region (residues 362 to 375) of the K$_v$1.2-2.1-2m and the K$_v$1.2-2.1 channel.
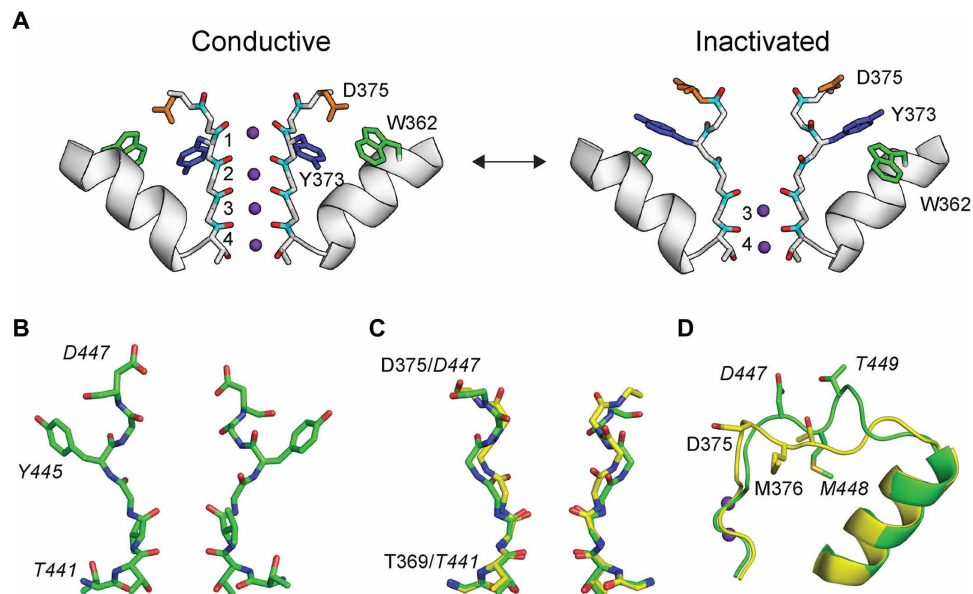
Fig. 5. C-type inactivation in a K$_v$ channel. (**A**) A model for the selectivity filter in the conductive and the C-type inactivated state. The conductive state of the selectivity filter is observed in the K$_v$1.2-2.1 channel (pdb: 2r9r), while the C-type inactivated state is based on the structure of the selectivity filter in the K$_v$1.2-2.1-3m channel. Two opposite subunits are shown. (**B**) Structure of the selectivity filter of the Shaker W434F channel (pdb: 7sj1). Residues *T441* to *D447* from two opposite subunits are shown in stick representation. (**C**) Superposition of the protein backbone of the selectivity filter of the K$_v$1.2-2.1-3m (residues 369 to 375, yellow) and the Shaker W434F channels (residues *441* to *447*, green) in shown. (**D**) Superposition of residues 369 to 391 of the K$_v$1.2-2.1-3m channel (yellow) with residues *441* to *463* of the Shaker W434F channel (green). Residues D375/*447*, M376/*448*, and T377/*449* are shown as sticks with the K$^+$ ions in the selectivity filter shown as purple spheres. Residues numbering in italics correspond to the Shaker channel.

conformational changes similar to that observed in the K$_v$1.2-2.1-3m and the Shaker W434F channel structure underlie inactivation or gating at the selectivity filter in diverse K$_v$ channels.

MATERIALS AND METHODS
Molecular biology
The K$_v$1.2-2.1 and the K$_v\beta$2.1 genes were a gift from R. MacKinnon (The Rockefeller University) (*3*). K$_v$1.2-2.1 gene was cloned into pAMV vector (provided by M. Zhou, Baylor College of Medicine) for electrophysiology experiments and into the pPicZ-C vector (Thermo Fisher Scientific) for protein expression in *Pichia pastoris*. Site-directed mutagenesis was carried out by polymerase chain reaction–based mutagenesis and confirmed through DNA sequencing. Complementary RNA (cRNA) was transcribed using the mMessage mMachine kit (Thermo Fisher Scientific) and purified using the RNeasy kit (Qiagen).

Electrophysiology
Xenopus laevis oocytes were provided by M. Danilchik (Oregon Health & Science University, protocol no. IP00000214) or purchased from Ecocyte Biosciences. Oocytes were injected with 50 nl (50 to 600 ng) of cRNA, and ionic currents were measured 1 to 4 days after injection using a two-electrode voltage clamp on an OC-725 amplifier (Warner). Recordings were carried out either in 100 mM K$^+$ [96 mM KCl, 2 mM NaCl, 5 mM Hepes-KOH, and 2 mM MgCl$_2$ (pH 7.5)] or in 1 mM K$^+$ solution [1 mM KCl, 117 mM NaCl, 0.3 mM CaCl$_2$, 1 mM MgCl$_2$, and 5 mM Hepes-NaOH (pH 7.5)]. Glass electrodes used were filled with 3 M KCl and had a resistance of 1 to 3 megaohms. Data were sampled at 10 kHz and filtered at

1 kHz. The time constants for inactivation were determined by fitting the decay in current to a single exponential. All data reported were collected from 5 to 10 oocytes and from at least three separate batches of oocytes.

Protein expression, purification, and crystallization
The K$_v$1.2-2.1-3m and K$_v$1.2-2.1-2m construct in the pPicZ plasmids carried an N-terminal His^{10} tag and a thrombin protease cleavage site. The K$_v$1.2-2.1-3m and K$_v$1.2-2.1-2m pPicZ plasmids were linearized with Bgl II and ligated with the K$_v\beta$ 2 gene (36 to 367 residues on a Bgl II/Bam HI DNA fragment). Plasmids with both the channel and the beta subunit were linearized with Pme I and transformed into *P. pastoris* strain (SMD1163) by electroporation. Transformants were selected on YPDS (yeast extract, peptone, dextrose, and sorbitol) (*44*) plates containing Zeocin (800 µg/ml). The transformants were grown in liquid culture and tested for expression using anti-His Western blotting (Proteintech). Transformants showing good expression were selected and stored as glycerol stocks at −80°C.

For protein expression, 10 ml of an overnight culture grown in YPD (*44*) medium with Zeocin (200 µg/ml) was used to inoculate 1 liter of BMGY [yeast nitrogen base, KPO$_4$ (pH 6.5), and glycerol] (*44*) medium with Zeocin (50 µg/ml) and grown at 30°C for 24 hours. The cells were then pelleted by centrifugation (1500*g*, 10 min) and transferred to BMMY medium [yeast nitrogen base, KPO$_4$ (pH 6.5), and methanol] (*44*) with Zeocin (25 µg/ml). After 24 hours, 0.5% (v/v) methanol was added to the culture to induce protein expression, and growth was continued for an additional 24 hours. The cells were then pelleted by centrifugation (4500*g*, 20 min) and frozen in liquid N$_2$ until use.

For purification, the frozen cells were lysed by milling (MM400, Retsch Inc.). Six cycles of milling at 25 Hz for 3 min were carried out. The cells were kept at low temperatures between milling cycles by cooling in liquid nitrogen. The cell powder obtained after milling was solubilized (1 g/5 ml) in 50 mM tris-HCl (pH 7.5), 150 mM KCl, 2 mM TCEP [tris(2-carboxyethyl)-phosphine hydrochloride], 10 mM β-mercaptoethanol (βme), deoxyribonuclease I (0.05 mg/ml), 1 mM MgCl₂, 1 mM phenylmethylsulfonyl fluoride, leupeptin (1 μg/ml), pepstatin (0.1 μg/ml), aprotinin (1 μg/ml), and soy trypsin inhibitor (0.1 mg/ml). The pH of the suspension was adjusted to 7.5 with KOH, and the membranes were solubilized with 1.5% (w/v) n-dodecyl-β-D-maltopyranoside (DDM) for 3 hours at room temperature. The unsolubilized material was separated by ultracentrifugation (100,000g, 50 min). The supernatant following ultracentrifugation was added to cobalt beads (1.5 ml of cobalt resin/40 ml) preequilibrated with column buffer [50 mM tris-HCl (pH 7.5), 150 mM KCl, 2 mM TCEP, 10 mM βme, and 5 mM DDM]. The bead slurry was overlaid with argon gas and incubated overnight at 4°C with gentle rotation. After incubation, the beads were collected on a column and washed with 20 volumes of column buffer containing lipids (0.1 mg/ml) [3:1:1 of POPC (1-palmitoyl-2-oleoyl-sn-glycero-3-phosphocholine):POPE (1-palmitoyl-2-oleoyl-sn-glycero-3-phosphoethanolamine):POPG (1-palmitoyl-2-oleoyl-sn-glycero-3-phosphoglycerol)] and 20 mM imidazole, and the bound protein was then eluted with 400 mM imidazole. The eluted protein was supplemented with 10 mM dithiothreitol (DTT), concentrated using a Millipore Amicon Ultra 100 K device, and further purified on a Superdex S200 column in 20 mM tris-HCl (pH 7.5), 150 mM KCl, 2 mM TCEP, 10 mM DTT, 1 mM EDTA, lipids (0.1 mg/ml) (3:1:1 of POPC:POPE:POPG), 3 mM Cymal-6, and 3 mM Cymal-7. The fractions containing both the channel and the beta subunits were pooled and concentrated to 15 mg/ml.

For crystallization, 8 mM CHAPS detergent (Anatrace) was added to the protein sample and incubated at room temperature for 45 min. Crystallization was carried out by the hanging drop vapor diffusion method using a crystallization solution of 100 mM tris-HCl (pH 8.2 to 8.8) and 26 to 36% polyethylene glycol 400 (PEG400) and set up using a Mosquito Crystal system (TTP Labtech). A 1:1 ratio of protein to crystallization solution was used for growing the K$_v$1.2-2.1-3m crystals, while a ratio of 2:1 was used for K$_v$1.2-2.1-2m. The rod-shaped crystals generally appeared after 4 to 5 days. For cryoprotection, the PEG400 concentration in the well solution was increased to 35% (if necessary) and incubated for an additional 24 hours. The crystals were harvested and frozen in liquid N₂.

Solving the K$_v$1.2-2.1-3m crystal structure

Diffraction data for the K$_v$1.2-2.1-3m crystals were collected at Advanced Photon Source (beamlines 23ID-B and 23ID-D). The crystals were sensitive to radiation damage. Multiple datasets were collected, processed using X-ray Detector Software (XDS) (45), and analyzed using Pointless (46) and Aimless (47). Sectors from the datasets that contained high-resolution diffraction data were merged using BLEND (48) to obtain a complete dataset of 3.35 Å. This dataset had a completeness of 100% in the outer shell (3.51 to 3.35) with an I/σ of 0.8 and a CC$_{1/2}$ of 0.55 along with minimal anisotropy (3.42 Å in h and k planes and 3.35 Å in l planes). The K$_v$1.2-2.1-3m crystallized in the same $P4\,2_1\,2$ space group as the K$_v$1.2-2.1 channel but with slightly smaller unit cell parameters (129.59, 129.59, and 278.48).

The R$_{free}$ flag from the dataset for the K$_v$1.2-2.1 structure (pdb: 2r9r) (3) was transferred to the K$_v$1.2-2.1-3m dataset before molecular

replacement. For molecular replacement, the K$_v$1.2-2.1 structure with the selectivity filter (residues 370 to 376), cofactors, lipids, and water molecules deleted was used as the search model. Molecular replacement was carried out using Phaser (49). The asymmetric unit consists of two copies of the channel and the beta subunits. The channel subunit consists of the TM and the T1 domains. The best molecular replacement solution obtained consisted of the TM domain of one channel subunit along with two T1 domains and two beta subunits. Attempts to place the TM region of the second channel subunit were not successful.

We refined the molecular replacement solution by Jellybody refinement in Refmac (50) followed by multiple cycles of manual structure adjustments using COOT (51) and refinement using Phenix (52). The electron density in the T1 domains and the beta subunits was very clear and allowed unambiguous placement of the protein chain into the electron density. Similarly, the TM5, pore helix, and the TM6 helices were easily modeled into the electron density. The electron density in the selectivity filter residues Y373 to D375 was weak, and so, these residues were not modeled at this stage. The electron density for the VSD was weak compared to the TM segments in the pore domain but was sufficient for the unambiguous placement of the TM1 to TM4 segments in the electron density. The electron density for the loops between the TM helices in the VSD was very poor, and so, these loops were not modeled. For the Y373-G374-D375 region of the selectivity filter, we calculated Polder (53) omit maps using Phenix, which allowed us to model the amino acid side chains for Y373 and D375. Electron density for the CO of G374 was not observed, and so, the placement is speculative. An omit map calculated at this stage showed clear density for the TM regions in the second channel molecule. We placed TM domain from the first channel molecule into this density and refined the structure by Jellybody refinement in Refmac followed by manual adjustments in COOT and further refinement in Phenix. The cofactor NAP (Nicotinamide-adenine-dinucleotide-phosphate) and ions/water in the selectivity filter were added. The final model includes residues 36 to 361 of the beta subunits (chains A and C). In the channel subunits (chains B and D), the model includes all the residues in the TM segments, while residues in the linker region connecting T1 domain and VSD (133 to 142 in B and 134 to 147 in D), the TM1-TM2 loop (192 to 217 in B and 191 to 218 in D), and the TM3-TM4 loop (273 to 286 in chains B and D) were not modeled. Figures were prepared using PyMOL (54) or Chimera (55). The solvent-accessible area for K$_v$1.2-2.1 and K$_v$1.2-2.1-3m was calculated using the Qt-PISA program in CCP4 (56). Annotation of the various regions of the pore domain in fig. S6 was carried out using DOG2.0 (57). Videos showing the morph between the conductive and the inactivated confirmation of the selectivity filter were recorded using UCSF Chimera (55).

REFERENCES AND NOTES

1. B. Hille, *Ion Channels of Excitable Membranes* (Sinauer Sunderland, 2001).
2. S. B. Long, E. B. Campbell, R. Mackinnon, Crystal structure of a mammalian voltage-dependent Shaker family K⁺ channel. *Science* **309**, 897–903 (2005).
3. S. B. Long, X. Tao, E. B. Campbell, R. MacKinnon, Atomic structure of a voltage-dependent K⁺ channel in a lipid membrane-like environment. *Nature* **450**, 376–382 (2007).

4. D. M. Kim, C. M. Nimigean, Voltage-gated potassium channels: A structural examination of selectivity and gating. *Cold Spring Harb. Perspect. Biol.* **8**, a029231 (2016).

5. H. T. Kurata, D. Fedida, A structural interpretation of voltage-gated potassium channel inactivation. *Prog. Biophys. Mol. Biol.* **92**, 185–208 (2006).

6. T. Hoshi, W. N. Zagotta, R. W. Aldrich, Biophysical and molecular mechanisms of Shaker potassium channel inactivation. *Science* **250**, 533–538 (1990).

7. T. Hoshi, W. N. Zagotta, R. W. Aldrich, Two types of inactivation in Shaker K$^+$ channels: Effects of alterations in the carboxy-terminal region. *Neuron* **7**, 547–556 (1991).

8. M. Zhou, J. Morais-Cabral, S. Mann, R. MacKinnon, Potassium channel receptor site for the inactivation gate and quaternary amine inhibitors. *Nature* **411**, 657–661 (2001).

9. C. Fan, N. Sukomon, E. Flood, J. Rheinberger, T. W. Allen, C. M. Nimigean, Ball-and-chain inactivation in a calcium-gated potassium channel. *Nature* **580**, 288–293 (2020).

10. T. Hoshi, C. M. Armstrong, C-type inactivation of voltage-gated K$^+$ channels: Pore constriction or dilation? *J. Gen. Physiol.* **141**, 151–160 (2013).

11. R. W. Aldrich Jr., P. A. Getting, S. H. Thompson, Mechanism of frequency-dependent broadening of molluscan neurone soma spikes. *J. Physiol.* **291**, 531–544 (1979).

12. J. Roeper, C. Lorra, O. Pongs, Frequency-dependent inactivation of mammalian A-type K$^+$ channel Kv1.4 regulated by Ca^{2+}/calmodulin-dependent protein kinase. *J. Neurosci.* **17**, 3379–3391 (1997).

13. R. MacKinnon, Nobel lecture. Potassium channels and the atomic basis of selective ion conduction. *Biosci. Rep.* **24**, 75–100 (2004).

14. Y. Zhou, J. H. Morais-Cabral, A. Kaufman, R. MacKinnon, Chemistry of ion coordination and hydration revealed by a K$^+$ channel-Fab complex at 2.0 A resolution. *Nature* **414**, 43–48 (2001).

15. V. Pau, Y. Zhou, Y. Ramu, Y. Xu, Z. Lu, Crystal structure of an inactivated mutant mammalian voltage-gated K$^+$ channel. *Nat. Struct. Mol. Biol.* **24**, 857–865 (2017).

16. F. I. Valiyaveetil, A glimpse into the C-type-inactivated state for a potassium channel. *Nat. Struct. Mol. Biol.* **24**, 787–788 (2017).

17. J. F. Cordero-Morales, L. G. Cuello, E. Perozo, Voltage-dependent gating at the KcsA selectivity filter. *Nat. Struct. Mol. Biol.* **13**, 319–322 (2006).

18. L. G. Cuello, V. Jogini, D. M. Cortes, E. Perozo, Structural mechanism of C-type inactivation in K$^+$ channels. *Nature* **466**, 203–208 (2010).

19. L. G. Cuello, D. M. Cortes, E. Perozo, The gating cycle of a K$^+$ channel at atomic resolution. *eLife* **6**, e28032 (2017).

20. P. K. Devaraneni, A. G. Komarov, C. A. Costantino, J. J. Devereaux, K. Matulef, F. I. Valiyaveetil, Semisynthetic K$^+$ channels show that the constricted conformation of the selectivity filter is not the C-type inactivated state. *Proc. Natl. Acad. Sci. U.S.A.* **110**, 15698–15703 (2013).

21. J. Lopez-Barneo, T. Hoshi, S. H. Heinemann, R. W. Aldrich, Effects of external cations and mutations in the pore region on C-type inactivation of Shaker potassium channels. *Receptors Channels* **1**, 61–71 (1993).

22. T. Baukrowitz, G. Yellen, Modulation of K$^+$ current by frequency and external [K$^+$]: A tale of two inactivation mechanisms. *Neuron* **15**, 951–960 (1995).

23. Y. Yang, Y. Yan, F. J. Sigworth, How does the W434F mutation block current in Shaker potassium channels? *J. Gen. Physiol.* **109**, 779–789 (1997).

24. J. F. Cordero-Morales, V. Jogini, S. Chakrapani, E. Perozo, A multipoint hydrogen-bond network underlying KcsA C-type inactivation. *Biophys. J.* **100**, 2387–2393 (2011).

25. E. Suarez-Delgado, T. G. Rangel-Sandin, I. G. Ishida, G. E. Rangel-Yescas, T. Rosenbaum, L. D. Islas, K$_v$1.2 channels inactivate through a mechanism similar to C-type inactivation. *J. Gen. Physiol.* **152**, e201912499 (2020).

26. X. Tao, R. MacKinnon, Functional analysis of Kv1.2 and paddle chimera Kv channels in planar lipid bilayers. *J. Mol. Biol.* **382**, 24–33 (2008).

27. S. J. Goodchild, H. Xu, Z. Es-Salah-Lamoureux, C. A. Ahern, D. Fedida, Basis for allosteric open-state stabilization of voltage-gated potassium channels by intracellular cations. *J. Gen. Physiol.* **140**, 495–511 (2012).

28. I. Utsunomiya, S. Tanabe, T. Terashi, S. Ikeno, T. Miyatake, K. Hoshi, K. Taguchi, Identification of amino acids in the pore region of Kv1.2 potassium channel that regulate its glycosylation and cell surface expression. *J. Neurochem.* **112**, 913–923 (2010).

29. T. Baukrowitz, G. Yellen, Use-dependent blockers and exit rate of the last ion from the multi-ion pore of a K$^+$ channel. *Science* **271**, 653–656 (1996).

30. L. Kiss, S. J. Korn, Modulation of C-type inactivation by K$^+$ at the potassium channel selectivity filter. *Biophys. J.* **74**, 1840–1849 (1998).

31. Y. Liu, M. E. Jurman, G. Yellen, Dynamic rearrangement of the outer mouth of a K$^+$ channel during gating. *Neuron* **16**, 859–867 (1996).

32. G. Yellen, D. Sodickson, T. Y. Chen, M. E. Jurman, An engineered cysteine in the external mouth of a K$^+$ channel allows inactivation to be modulated by metal binding. *Biophys. J.* **66**, 1068–1075 (1994).

33. H. S. Krovetz, H. M. VanDongen, A. M. VanDongen, Atomic distance estimates from disulfides and high-affinity metal-binding sites in a K$^+$ channel pore. *Biophys. J.* **72**, 117–126 (1997).

34. K. L. Choi, R. W. Aldrich, G. Yellen, Tetraethylammonium blockade distinguishes two inactivation mechanisms in voltage-activated K$^+$ channels. *Proc. Natl. Acad. Sci. U.S.A.* **88**, 5092–5095 (1991).

35. A. Cha, F. Bezanilla, Characterizing voltage-dependent conformational changes in the Shaker K$^+$ channel with fluorescence. *Neuron* **19**, 1127–1140 (1997).

36. C. S. Gandhi, E. Loots, E. Y. Isacoff, Reconstructing voltage sensor-pore interaction from a fluorescence scan of a voltage-gated K$^+$ channel. *Neuron* **27**, 585–595 (2000).

37. E. Loots, E. Y. Isacoff, Molecular coupling of S4 to a K$^+$ channel's slow inactivation gate. *J. Gen. Physiol.* **116**, 623–636 (2000).

38. H. P. Larsson, F. Elinder, A conserved glutamate is important for slow inactivation in K$^+$ channels. *Neuron* **27**, 573–583 (2000).

39. A. Mathie, E. Al-Moubarak, E. L. Veale, Gating of two pore domain potassium channels. *J. Physiol.* **588**, 3149–3156 (2010).

40. M. Lolicato, A. M. Natale, F. Abderemane-Ali, D. Crottes, S. Capponi, R. Duman, A. Wagner, J. M. Rosenberg, M. Grabe, D. L. Minor Jr., K$_{2P}$ channel C-type gating involves asymmetric selectivity filter order-disorder transitions. *Sci. Adv.* **6**, eabc9174 (2020).

41. B. Li, R. A. Rietmeijer, S. G. Brohawn, Structural basis for pH gating of the two-pore domain K$^+$ channel TASK2. *Nature* **586**, 457–462 (2020).

42. X.-F. Tan, C. Bae, R. Stix, A. I. Fernández-Mariño, K. Huffer, T.-H. Chang, J. Jiang, J. D. Faraldo-Gómez, K. J. Swartz, Structure of the Shaker Kv channel and mechanism of slow C-type inactivation. *bioRxiv* 2021.2009.2021.461258 , (2022).

43. C. Boiteux, D. J. Posson, T. W. Allen, C. M. Nimigean, Selectivity filter ion binding affinity determines inactivation in a potassium channel. *Proc. Natl. Acad. Sci. U.S.A.* **117**, 29968–29978 (2020).

44. M. Weidner, M. Taupp, S. J. Hallam, Expression of recombinant proteins in the methylotrophic yeast Pichia pastoris. *J. Vis. Exp.* **36**, 1862 (2010).

45. W. Kabsch, XDS. *Acta Crystallogr. D Biol. Crystallogr.* **66**, 125–132 (2010).

46. P. R. Evans, An introduction to data reduction: Space-group determination, scaling and intensity statistics. *Acta Crystallogr. D Biol. Crystallogr.* **67**, 282–292 (2011).

47. P. R. Evans, G. N. Murshudov, How good are my data and what is the resolution? *Acta Crystallogr. D Biol. Crystallogr.* **69**, 1204–1214 (2013).

48. P. Aller, T. Geng, G. Evans, J. Foadi, Applications of the BLEND software to crystallographic data from membrane proteins. *Adv. Exp. Med. Biol.* **922**, 119–135 (2016).

49. A. J. McCoy, R. W. Grosse-Kunstleve, P. D. Adams, M. D. Winn, L. C. Storoni, R. J. Read, Phaser crystallographic software. *J. Appl. Cryst.* **40**, 658–674 (2007).

50. G. N. Murshudov, P. Skubak, A. A. Lebedev, N. S. Pannu, R. A. Steiner, R. A. Nicholls, M. D. Winn, F. Long, A. A. Vagin, REFMAC5 for the refinement of macromolecular crystal structures. *Acta Crystallogr. D Biol. Crystallogr.* **67**, 355–367 (2011).

51. P. Emsley, K. Cowtan, Coot: Model-building tools for molecular graphics. *Acta Crystallogr. D Biol. Crystallogr.* **60**, 2126–2132 (2004).

52. P. D. Adams, P. V. Afonine, G. Bunkoczi, V. B. Chen, I. W. Davis, N. Echols, J. J. Headd, L. W. Hung, G. J. Kapral, R. W. Grosse-Kunstleve, A. J. McCoy, N. W. Moriarty, R. Oeffner, R. J. Read, D. C. Richardson, J. S. Richardson, T. C. Terwilliger, P. H. Zwart, PHENIX: A comprehensive Python-based system for macromolecular structure solution. *Acta Crystallogr. D Biol. Crystallogr.* **66**, 213–221 (2010).

53. D. Liebschner, P. V. Afonine, N. W. Moriarty, B. K. Poon, O. V. Sobolev, T. C. Terwilliger, P. D. Adams, Polder maps: Improving OMIT maps by excluding bulk solvent. *Acta Crystallogr D Struct Biol* **73**, 148–157 (2017).

54. W. L. Dealno, *The PyMol Molecular Graphics System* (DeLano Scientific, 2002).

55. E. F. Pettersen, T. D. Goddard, C. C. Huang, G. S. Couch, D. M. Greenblatt, E. C. Meng, T. E. Ferrin, UCSF Chimera—A visualization system for exploratory research and analysis. *J. Comput. Chem.* **25**, 1605–1612 (2004).

56. E. Krissinel, K. Henrick, Inference of macromolecular assemblies from crystalline state. *J. Mol. Biol.* **372**, 774–797 (2007).

57. J. Ren, L. Wen, X. Gao, C. Jin, Y. Xue, X. Yao, DOG 1.0: Illustrator of protein domain structures. *Cell Res.* **19**, 271–273 (2009).